

Holocene ENSO-related cyclic storms recorded by magnetic minerals in speleothems of central China

Zongmin Zhu^{a,b,1}, Joshua M. Feinberg^b, Shucheng Xie^a, Mark D. Bourne^b, Chunju Huang^a, Chaoyong Hu^a, and Hai Cheng^c

^aState Key Laboratory of Biogeology and Environmental Geology, School of Earth Sciences, China University of Geosciences, Wuhan 430074, China; ^bInstitute for Rock Magnetism, University of Minnesota, Minneapolis, MN 55455; and ^cInstitute of Global Environmental Change, Xi'an Jiaotong University, Xi'an 710049, China

Edited by Lisa Tauxe, University of California, San Diego, La Jolla, CA, and approved November 28, 2016 (received for review July 5, 2016)

Extreme hydrologic events such as storms and floods have the potential to severely impact modern human society. However, the frequency of storms and their underlying mechanisms are limited by a paucity of suitable proxies, especially in inland areas. Here we present a record of speleothem magnetic minerals to reconstruct paleoprecipitation, including storms, in the eastern Asian monsoon area over the last 8.6 ky. The geophysical parameter $IRM_{soft-flux}$ represents the flux of soil-derived magnetic minerals preserved in stalagmite HS4, which we correlate with rainfall amount and intensity. $IRM_{soft-flux}$ exhibits relatively higher values before 6.7 ky and after 3.4 ky and lower values in the intervening period, consistent with regional hydrological changes observed in independent records. Abrupt enhancements in the flux of pedogenic magnetite in the stalagmite agree well with the timing of known regional paleofloods and with equatorial El Niño–Southern Oscillation (ENSO) patterns, documenting the occurrence of ENSO-related storms in the Holocene. Spectral power analyses reveal that the storms occur on a significant 500-y cycle, coincident with periodic solar activity and ENSO variance, showing that reinforced (subdued) storms in central China correspond to reduced (increased) solar activity and amplified (damped) ENSO. Thus, the magnetic minerals in speleothem HS4 preserve a record of the cyclic storms controlled by the coupled atmosphere–oceanic circulation driven by solar activity.

storms | paleoprecipitation | speleothems | environmental magnetism | paleoclimate

Carbonate cave deposits are attractive archives for reconstructing changes in past climate because they can provide high-resolution and, in most cases, continuous records. Measurements of oxygen and carbon stable isotopes in speleothems are used routinely to recover information about environmental changes, including monsoon intensity in monsoon-impacted regions (1), although they are highly debated (2–6). Monsoon-driven storms are a common example of extreme precipitation events that can cause widespread flooding and create hazardous conditions for communities and their infrastructure. Identification of storms and elevated precipitation in prehistoric times is thus critical for understanding regional hydrological changes and testing the potential mechanisms that may influence them. Despite their high temporal resolution, speleothems remain an underused tool for assessing regional storm and flood frequency throughout the Holocene, and may offer unique insights into the long-term processes that drive changes in the frequency of such events.

Magnetic minerals, transported by groundwater from soils overlying the cave system, are incorporated into speleothems as they grow, and long-term changes in precipitation can be recorded by magnetic minerals in speleothems (7–11). Recent advances in measurement sensitivity have opened up speleothems as viable archives of magnetic information (7, 11). Here, we examine whether such magnetic records can provide an opportunity to identify extreme precipitation events, such as storms, by measurement of magnetic minerals in a stalagmite from central China,

a region strongly influenced by both the Eastern Asian and Indian monsoon systems. One-hundred-and-fifteen cubic specimens ($2 \times 2 \times 2$ cm) were collected from a 2.5-m-tall stalagmite (HS4) from Heshang Cave ($30^{\circ}27'N$, $110^{\circ}25'E$), central China, for magnetic measurements (Fig. 1; sampling methods are well documented in ref. 10). U–Th dating, combined with layer counting, indicated that the stalagmite grew continuously over the last 9.0 ky (12).

Soil-Derived Magnetic Minerals in Stalagmite HS4 and Their Hydrological Implication

Magnetite, goethite, and hematite/maghemite were identified in our samples. Coercivity unmixing analyses were conducted on specimens from stalagmite HS4 by alternating field (AF) demagnetization of an isothermal remanent magnetization ($IRM_{1.15T}$) induced by a 1.15-T direct current (dc) field (*Methods*). For each sample, $\sim 90\%$ of the $IRM_{1.15T}$ is carried by a mineral population with an ~ 20 -mT median destructive field (MDF) and a dispersion parameter (DP) of ~ 0.4 (Fig. 2). A small proportion ($<4\%$) of the total remanence is carried by a lower coercivity, or magnetically very “soft,” component with an MDF < 5 mT (Fig. 2), which is likely to be coarse, multidomain magnetic particles. Magnetic particles were extracted from stalagmite HS4 for more detailed mineralogical analyses, including low-temperature magnetic measurements and electronic microscopy (*Methods*). The presence of magnetite in HS4 was confirmed in all of the magnetic extracts by observation of an abrupt decrease in magnetization at ~ 120 K, identified as the Verwey transition, during low-temperature cycling of thermal remanent magnetization (TRM) (Fig. S1). Low-temperature magnetometry also provided evidence for the

Significance

High-resolution reconstructions of storm history and storms' underlying mechanisms in inland areas are critical but limited by a paucity of suitable paleoproxies. Here we use soil-derived magnetic minerals preserved in a stalagmite as a new paleo-hydrological proxy. This proxy enables us to rebuild decadal resolution storm records in the eastern Asian monsoon area since 8.6 ky. Variance of storms in central China was found to exhibit close correlation with El Niño–Southern Oscillation activity at millennial and centennial time scales, and also occur on a significant 500-y cycle related to periodic solar activity. These findings shed light on the forecasting of future floods and improve our understanding of the potential mechanism of strong precipitation in monsoon regions.

Author contributions: Z.Z. designed research; Z.Z. performed research; J.M.F., S.X., and M.D.B. contributed new reagents/analytic tools; Z.Z., J.M.F., S.X., M.D.B., C. Huang, C. Hu, and H.C. analyzed data; and Z.Z., J.M.F., and S.X. wrote the paper.

The authors declare no conflict of interest.

This article is a PNAS Direct Submission.

¹To whom correspondence should be addressed. Email: zhumin@cug.edu.cn.

This article contains supporting information online at www.pnas.org/lookup/suppl/doi:10.1073/pnas.1610930114/-DCSupplemental.

rainfall and wetter intervals, it may also record discrete high-intensity precipitation events. In contrast to pedogenic processes that slowly increase the amount of pedogenic ferrimagnetic minerals within soils, large storms can dramatically increase the energy of groundwater in karst regions within a very short time, causing an abrupt increase in the transportation of heavy minerals to the cave system and, in turn, an abrupt increase in the amount of allochthonous particles preserved in stalagmites. We therefore relate abrupt enhancements in $IRM_{\text{soft-flux}}$ to increases in magnetite flux resulting from an increased frequency of extreme precipitation events such as storms.

Long-Term Hydrological Variation and Storms

The mean $IRM_{\text{soft-flux}}$ is relatively low ($5.3 \times 10^{-10} \text{ Am}^2 \cdot \text{y}^{-1}$) between 6.7 ky and 3.4 ky, compared with higher values ($14.9 \times 10^{-10} \text{ Am}^2 \cdot \text{y}^{-1}$) before 6.7 ky and after 3.4 ky (Fig. 3A). This three-interval pattern is in good agreement with local water levels recorded by the accumulation rate of aerobic hopanoids in Dajiuhe peatland, a site about 120 km north of Heshang cave (7) (Fig. 3C). The two wet periods (before 6.7 ky and after 3.4 ky) also agree well with the highest lake water level in the middle and lower reaches of Yangtze River, which occurred between 8.0 ky

and 7.0 ky and after 3.0 ky (19). The carbon isotope composition of the soil-derived acid-soluble organic matter ($\delta^{13}\text{C}_{\text{ASOM}}$) in the HS4 stalagmite (Fig. 3B and ref. 20) also records a pattern comparable to $IRM_{\text{soft-flux}}$ on a millennial scale, with less negative $\delta^{13}\text{C}_{\text{ASOM}}$ values during the two wet periods. These consistencies between the three different records suggest that $IRM_{\text{soft-flux}}$ is a reliable and accurate indicator of regional hydrological changes in central China throughout the Holocene.

A detailed comparison of the magnetic signals and oxygen compositions of carbonate from the HS4 stalagmite is shown in Fig. S3 and does not show any significant correlation. It is well known that $\delta^{18}\text{O}$ in cave sediments is controlled by a variety of factors, including rainfall amount, cave temperature, local evaporation, the $\delta^{18}\text{O}$ of the sources (the Indian Ocean or/and the West Pacific Ocean), and the transport distance from the sources (21, 22). Models and modern observations have shown that variations in vapor sources rather than in the precipitation amount (1) dominated the speleothems $\delta^{18}\text{O}$ records in the East Asian monsoon (EAM) area (2–6). Consequently, converting stalagmite $\delta^{18}\text{O}$ records into a quantitative assessment of past rainfall amount, including that arising from typhoon sources, is very difficult in the EAM region (12), and it is therefore unsurprising that

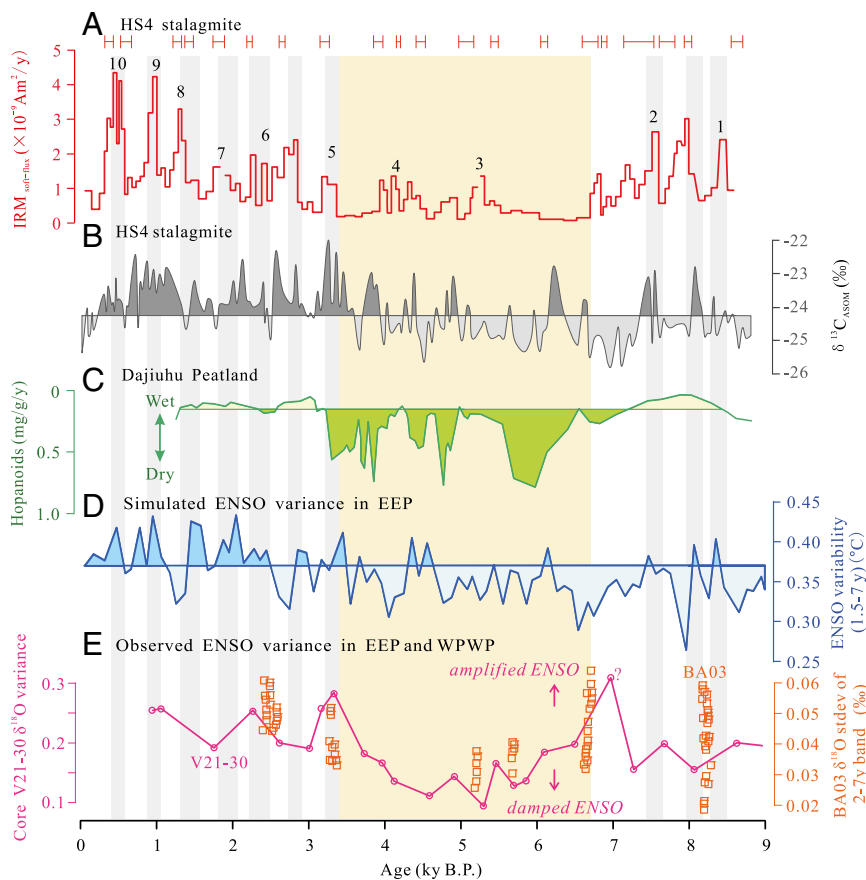


Fig. 3. Hydrological conditions in central China and ENSO strength. (A) $IRM_{\text{soft-flux}}$ in stalagmite HS4. Peaks in $IRM_{\text{soft-flux}}$ indicate intervals with increased extreme precipitation events (this study), numbers 1 through 10 indicate the flooding events reported near the research area (23–28). U–Th dating errors (12) are shown on the top of $IRM_{\text{soft-flux}}$ curve as red line segments. (B) The carbon isotope composition of the acid-soluble soil-derived organic matter ($\delta^{13}\text{C}_{\text{ASOM}}$) of HS4 stalagmite. Although affected by multiple factors, more (less) negative $\delta^{13}\text{C}_{\text{ASOM}}$ was correlated with dry (wet) climate (20). (C) Hopanoid accumulation rate in Dajiuhe peatland. High (low) accumulation rates correlate with dry (wet) intervals (7). (D) Simulated ENSO amplitude in 100-y window based on observation data [shown as SD of Nino3.4 (a region bounded by 5°N to 5°S , from 170°W to 120°W) interannual (1.5 y to 7 y) sea surface temperature variability] (39). (E) Observed ENSO variability from stalagmite BA03 (open squares) (33) and foraminiferal $\delta^{18}\text{O}$ (open circles) (34). BA03 $\delta^{18}\text{O}$ values are calculated based on the SD of the 2- to 7-y band in overlapping 30-y windows and indicate the ENSO variance in WPWP region. Foraminiferal $\delta^{18}\text{O}$ is retrieved from deep-sea sediments in core V21-30 located at EEP region (cold tongue of ENSO activity), and is established on single tests in each 1-cm stratum with an age uncertainty of several hundred years (34). The question mark indicates a questionable $\delta^{18}\text{O}$ value at 7.0 ky (mentioned in ref. 34). Comparison of peaks in $IRM_{\text{soft-flux}}$ and ENSO variance are indicated by gray bars. Vertical yellow bar indicates the regional dry period (6.7–3.4 ky).

there is no significant correlation between the $\delta^{18}\text{O}$ records and our magnetic signal.

The $\text{IRM}_{\text{soft-flux}}$ record shows pulses of abrupt, centennial-scale enhancement throughout the HS4 stalagmite. These abrupt enhancements are particularly strong during the two wet intervals (after 3.4 ky and before 6.7 ky), and are subdued during the dry interval between them. We interpret these pulses of enhanced $\text{IRM}_{\text{soft-flux}}$ to represent intervals of increased storm frequency/strength. For comparison, we compiled previously published histories of flood deposits preserved in the middle reaches of Yangtze River, and 10 paleoflood events could be recognized during the past 9.0 ky, occurring at 9,000–8,400 y B.P. (23, 24), 7500–7200 y B.P. (25), 5500–5000 y B.P. (26), 4200–4000 y B.P. (23, 27), 3200–2800 y B.P. (23–25), 2600–2200 y B.P. (28), 1900–1700 y B.P. (23, 27), 1200 y B.P. (28), 1000–800 y B.P. (26, 28), and 590 ± 50 y B.P. (28), respectively. These paleoflood events are identified in peaks in $\text{IRM}_{\text{soft-flux}}$ in Fig. 3A and indicate periods of elevated precipitation (23, 25, 28). Extreme paleofloods became more frequent after 2.2 ky and reached a maximum frequency between 1.0 ky and the present day (29), coincident with the two highest pulses of the $\text{IRM}_{\text{soft-flux}}$ value of HS4 stalagmite. In contrast, the pronounced aridity event induced by the abrupt cooling event in the North Atlantic region at 8.2 ky (30) is coincident with the weak $\text{IRM}_{\text{soft-flux}}$ value of HS4 stalagmite. The $\delta^{13}\text{C}_{\text{ASOM}}$ exhibits a similar variance to $\text{IRM}_{\text{soft-flux}}$ on a millennial scale, but not on a centennial scale; this may be due to the effects of temperature and vegetation on $\delta^{13}\text{C}_{\text{ASOM}}$ in addition to precipitation (20).

Close Correlation Between El Niño–Southern Oscillation and Storms in Central China

The occurrence of modern-day storms in the middle reaches of Yangtze River is related to the strength of El Niño–Southern Oscillation (ENSO) (31), especially the El Niño events (32). Although paleo-ENSO records are difficult to reconstruct, particularly in the early Holocene (33–35), our $\text{IRM}_{\text{soft-flux}}$ record appears to be consistent with paleo-ENSO proxies available for the Holocene. Geological data and climate models document a mid-Holocene reduction in ENSO intensity and fewer El Niño-related flood events (33, 34, 36–38) (Fig. 3D and E). This finding is consistent with lower $\text{IRM}_{\text{soft-flux}}$ values, which indicates fewer storms between 6.7 ky and 3.4 ky. Although the Holocene ENSO might show different spatial patterns (36), $\delta^{18}\text{O}$ variances of foraminifera (34) (open circles in Fig. 3E) and stalagmite BA03 (33) (open squares in Fig. 3E) support strong ENSO activity in both the eastern equatorial Pacific (EEP) and western Pacific warm pool (WPWP) regions during the early and later Holocene, which is broadly consistent with the frequent storms before 6.7 ky and after 3.4 ky indicated by the $\text{IRM}_{\text{soft-flux}}$ record. Of particular importance is that, during the relatively strong ENSO periods (the early and later Holocene), $\text{IRM}_{\text{soft-flux}}$ shows an increased frequency of enhancement pulses, and the peaks of $\text{IRM}_{\text{soft-flux}}$ during those periods broadly correspond to the peaks of the observed and modeled ENSO variances in the EEP region (33, 39) (Fig. 3D and E). This would suggest that stronger ENSO can increase the frequency of extreme precipitation events, such as storms, in central China.

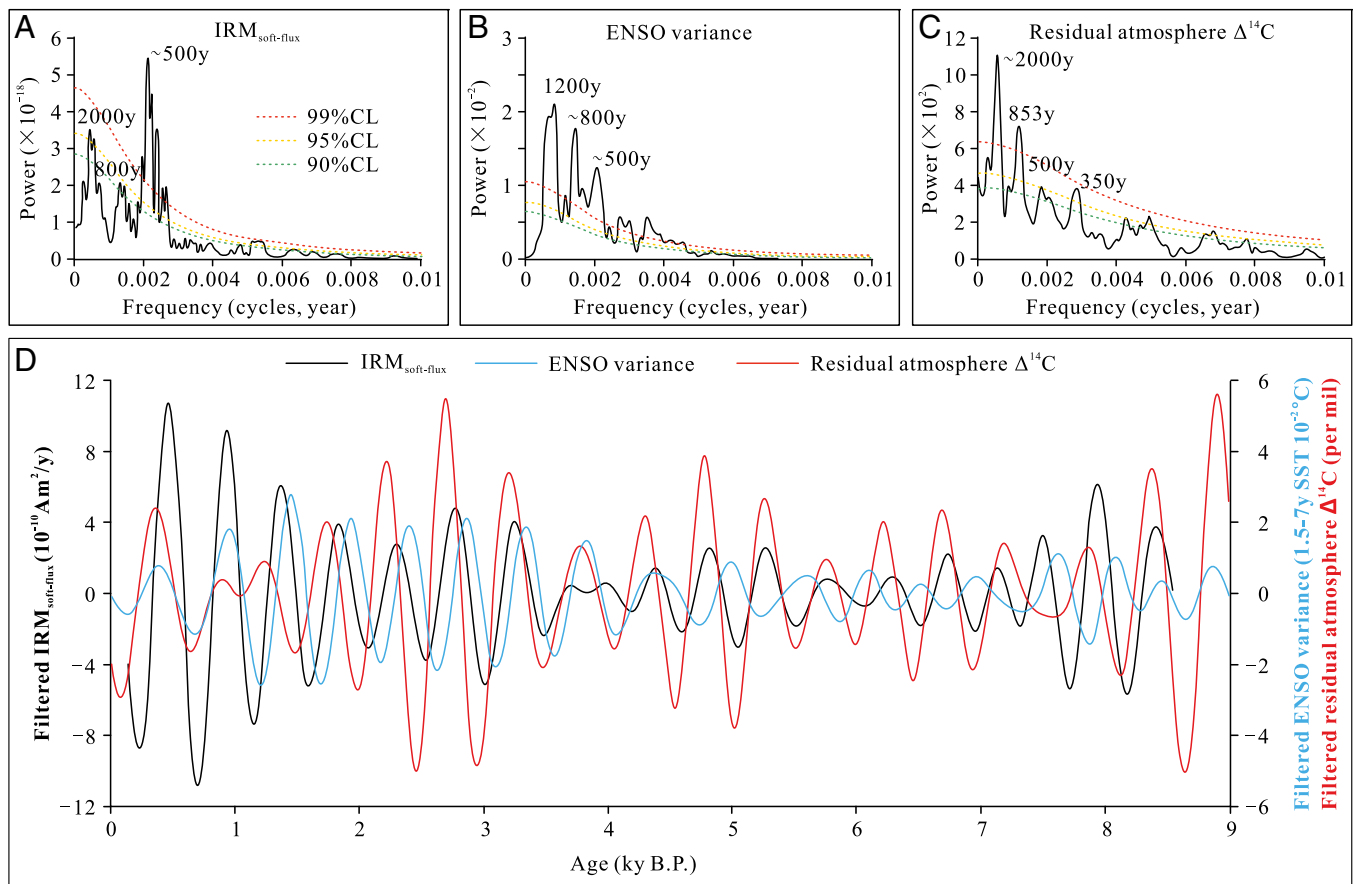


Fig. 4. Power analysis of $\text{IRM}_{\text{soft-flux}}$ of HS4, ENSO variance, and solar irradiance parameter [residual atmospheric $\Delta^{14}\text{C}$ from global tree ring records (46)]. (A–C) Power spectra of (A) $\text{IRM}_{\text{soft-flux}}$ (this study), (B) ENSO variance (39), and (C) residual atmosphere $\Delta^{14}\text{C}$ (46). Red, orange, and green dashed lines are 99%, 95%, and 90% confidence level (CL) respectively. (D) $\text{IRM}_{\text{soft-flux}}$ (black), ENSO variance (blue), and residual atmosphere $\Delta^{14}\text{C}$ (red) after 500-y band-pass filtering. Higher $\Delta^{14}\text{C}$ values correspond to periods of lower solar activity.

Some discrepancies do exist between the two ENSO records (simulated and observed) and the storms inferred by our magnetic record, which might arise from limitations inherent within the simulated and observed ENSO records. The simulated ENSO variability is based on modern observations, which means that the simulation becomes less reliable with increasing age. It might provide a good comparison for variations in frequency, but modeled changes in the amplitude become less reliable with increasing age. This tendency explains why our magnetic record shows similar cyclic variation to the simulated ENSO record (39), but shows inconsistent amplitude variation, particularly in the early Holocene (Fig. 3D). Further, the previously published data for the observed ENSO record display a comparatively low temporal resolution and a large uncertainty in age (33, 34). The observed ENSO record cannot provide a detailed comparison, but it does show the same three-interval features observed in the magnetic data (i.e., elevated during 9–6.7 ky, and 3.4–0 ky, but decreased during 6.7–3.4 ky) (Fig. 3E). Finally, the compilation of flooding events (23–29) in central China confirms the robustness of our magnetic profile as an ENSO record within the age uncertainties denoted in Fig. 3.

Five-Hundred-Year Periodicity of Storms and Its Forcing

Spectral analysis of the detrended $IRM_{soft-flux}$ record and modeled ENSO variance data (from ref. 39) reveal that they both exhibit a centennial cycle centered at ~500 y with a confidence level of greater than 99% (Fig. 4A and B). The 500-y cycle is a significant component of solar activity periodic variations (40, 41) (Fig. 4C), which can control Earth surface temperature variability and alter atmospheric and oceanic circulation (42–45). The 500-y cycle of storms in central China is generally in an antiphase relationship with solar activity, indicated by the residual atmospheric $\Delta^{14}C$ from global tree ring records (46) during the past 8.6 ky, where higher $IRM_{soft-flux}$ values (representing storms) are associated with low solar irradiation (larger $\Delta^{14}C$). The correlation between 500-y periodic storms and the ENSO variance is positive in the wet periods (the early and later Holocene), but it changes to a negative correlation in the dry period (the mid-Holocene) when the ENSO is damped and in a more La Niña-like state according to the observed data (33, 34).

Our results show that strong/frequent storms in central China are broadly consistent with weak solar irradiation as well as strong ENSO activities. Solar activity can modulate the EAM system and thereby affect precipitation in central China. Decreased solar irradiance can weaken the Asian summer monsoon (41, 43), which, in turn, could cause the convergence zone, the Mei-yu Front, where warm–moist, tropical–subtropical air meets the cooler continental air mass, to move southward toward the Yangtze River valley (47) and hover around this area. This southward movement could move preexisting storm centers closer to Heshang cave or, alternatively, increase the frequency of storms regionally. Although there are multiple controls on ENSO (39), its long-term variability is closely related to secular solar activity variations, and both the intensity and frequency of El Niño events, which result in flooding in east and central China (32), are high at secular solar minimum and low at secular solar maximum (48). Thus, solar radiation, ENSO activity, and coupled atmospheric–oceanic variation may therefore control the occurrence of ENSO-related storms in central China. The delayed response of storms in central China to the mature ENSO (48), and/or the different age modes of those two data series, could probably result in the small phase shift between ENSO variations and storms shown in Fig. 4D. Reduced ENSO activity during the dry mid-Holocene was not strong enough to affect the storms in central China, which might explain their weak relationship during this interval.

Methods

Sampling. One-hundred-and-fifteen environmental magnetism specimens (2-cm cubes) were cut sequentially from the core of the stalagmite where

growth layers accumulated in a nearly horizontal orientation (10) (Fig. S1). Four soil samples were collected from the B horizon of soil capping Heshang cave. Eight representative HS4 samples distributed across the whole time series were chosen for more advanced magnetic mineralogy analyses.

Extraction of Magnetic Minerals from Stalagmite HS4. To obtain unambiguous magnetic measurements and conduct morphological analyses on the magnetic particles, we dissolved fragments of stalagmite HS4 and extracted the magnetic minerals. The acetate buffer solution [4:1 (vol/vol) of 2 M acetic acid and 1 M sodium acetate] recommended by Perkins (16) was used for stalagmite dissolution. The extracting procedure followed that of Strehlau et al. (49).

$IRM_{soft-flux}$. All specimens were given an IRM using a 1-T dc field, and their remanences were signed as IRM_{1T} ; subsequently, the specimens were subjected to a 0.3-T dc field in the opposite direction (“backfield”) to produce another remanence signed as $IRM_{0.3T}$. Then $|IRM_{soft}|$ is defined as $0.5 \times (|IRM_{1T}| + |IRM_{0.3T}|)$. To eliminate the effect of variation on the stalagmite’s growth rate, $|IRM_{soft}|$ measurements were normalized using the age duration of each sample to give $IRM_{soft-flux}$ (Table S1), which represents the amount of soil-originated magnetic minerals preserved in stalagmite HS4 per year. Remanent magnetizations were imparted using a 2G Enterprises 670M long-core pulse magnetizer and were measured using a 2G U-channel cryogenic SQUID (superconducting quantum interference device) magnetometer.

Magnetic Mineralogy Analyses. IRMs were imparted to eight HS4 samples and four soil samples using a 1.15-T dc field and then progressively degaussed in AFs up to a maximum of 170 mT. The first derivatives of the demagnetization data were used to perform coercivity unmixing analyses to identify magnetic mineral components on the basis of their MDF and DP, calculated following the methods described in ref. 50. The contribution of the very soft component is represented by the portion of the IRM demagnetized following application of a 5-mT AF, and that of the pedogenic magnetite is indicated by the component of the IRM demagnetized between the application of a 20-mT and 5-mT AF. The ratio of the two soft components’ relative contributions was then calculated, and is 0.2 for almost all of the stalagmites samples and for all of the soil samples.

The low-temperature magnetic behavior of the samples extracted was examined using a Quantum Designs Magnetic Properties Measurement System (MPMS-5S). We used the goethite-pretreatment low-temperature measure sequence designed by Guyodo et al. (51) to target weak magnetic minerals such as goethite and hematite. Detailed protocols are provided in Fig. S1.

Electron Microscopy Analyses. The morphology of the extracted magnetic particles was observed using a scanning electron microscope (SEM) and a transmission electron microscope (TEM). The extracted magnetic particles were deposited onto carbon-coated adhesive tape, and then analyzed with a JSM-35CF SEM (Japanese Electronics Co., Ltd.). The elemental composition of magnetic minerals was measured using energy dispersive spectroscopy (EDS). For TEM analysis, magnetic particles were suspended in a solution of colloidal and isoamyl acetate [1:4 (vol/vol)] via 10 min of ultrasonic vibrating, and then two to three drops of the suspension were dropped into a bowl of pure water. A thin film then formed on the surface of the water, and a portion of this film was then applied to a TEM support grid, dried, and carbon-coated for TEM analyses using a Philips CM12/5 TEM. Further elemental analysis was provided by Philips PV9760 Energy Dispersive X-ray Analyzer attached to the Philips CM12/5 TEM. Photomicrographs collected from the SEM and TEM were obtained at operating voltages of 1.5 and 1.2 kv, respectively.

ACKNOWLEDGMENTS. We thank Mike Jackson, Peter Solheid, Bruce Moskowitz, and Dario Bilardello (Institute for Rock Magnetism, University of Minnesota) for their support on magnetic measurements and constructive discussions. We appreciate the warm-hearted assistance in magnetic measurements by Prof. Qingsong Liu and Dr. Huafeng Qing (Chinese Academy of Sciences). We thank Dr. Jennifer H. Strehlau (Department of Chemistry, University of Minnesota) for her help in extracting the magnetic minerals from stalagmite HS4. We also thank the anonymous reviewers for their careful work and thoughtful suggestions that have helped improve this paper substantially. The research was financially supported by the National Natural Science Foundation of China (Grants 41674072 and 41322013), State Key R&D program of China (Grant 2016YFA0601100), and the 111 program (National Bureau for Foreign Experts and the Ministry of Education of China, Grants B08030 and B14031). This is contribution #1511 of the Institute for Rock Magnetism, which is funded by the National Science Foundation Division of Earth Sciences Instruments and Facilities Program.

1. Wang YJ, et al. (2001) A high-resolution absolute-dated late Pleistocene Monsoon record from Hulu Cave, China. *Science* 294(5550):2345–2348.
2. Pausata F, Battisti D, Nisancioglu K, Bitz C (2011) Chinese stalagmite $\delta^{18}\text{O}$ controlled by changes in the Indian monsoon during a simulated Heinrich event. *Nat Geosci* 4: 474–480.
3. Conroy JL, Overpeck JT (2011) Regionalization of present-day precipitation in the greater monsoon region of Asia. *J Clim* 24(15):4073–4095.
4. Maher B, Thompson R (2012) Oxygen isotopes from Chinese caves: Records not of monsoon rainfall but of circulation regime. *J Quat Sci* 27(6):615–624.
5. Tan M (2014) Circulation effect: Response of precipitation $\delta^{18}\text{O}$ to the ENSO cycle in monsoon regions of China. *Clim Dyn* 42(3):1067–1077.
6. Thomas EK, et al. (2016) Heterodynes dominate precipitation isotopes in the East Asian monsoon region, reflecting interaction of multiple climate factors. *Earth Planet Sci Lett* 455:196–206.
7. Xie SC, et al. (2013) Concordant monsoon-driven postglacial hydrological changes in peat and stalagmite records and their impacts on prehistoric cultures in central China. *Geology* 41(8):827–830.
8. Lascu I, Feinberg JM (2011) Speleothem magnetism. *Quat Sci Rev* 30(23–24): 3306–3320.
9. Strauss BE, et al. (2013) The origin of magnetic remanence in stalagmites: Observations from electron microscopy and rock magnetism. *Geochem Geophys Geosyst* 14(12):5006–5025.
10. Zhu ZZ, et al. (2012) Magnetic fabric of stalagmites and its formation mechanism. *Geochem Geophys Geosyst* 13(6):Q06006.
11. Bourne MD, et al. (2015) Long-term changes in precipitation recorded by magnetic minerals in speleothems. *Geology* 43(7):595–598.
12. Hu C, et al. (2008) Quantification of Holocene Asian monsoon rainfall from spatially separated cave records. *Earth Planet Sci Lett* 266(3–4):221–232.
13. Egli R (2004) Characterization of individual rock magnetic components by analysis of remanence curves, 1. unmixing natural sediments. *Stud Geophys Geod* 48(2):391–446.
14. Geiss CE, Zanner CW (2006) How abundant is pedogenic magnetite? Abundance and grain size estimates for loessic soils based on rock magnetic analyses. *J Geophys Res* 111(B12):B12S21.
15. Perkins AM, Maher BA (1993) Rock magnetic and palaeomagnetic studies of British speleothems. *J Geomag Geoelectr* 45(2):143–153.
16. Perkins AM (1996) Observations under electron microscopy of magnetic minerals extracted from speleothems. *Earth Planet Sci Lett* 139(1–2):281–289.
17. Maher BA, Thompson R (1995) Paleorainfall reconstructions from pedogenic magnetic susceptibility variations in the Chinese loess and paleosols. *Quat Res* 44(3): 383–391.
18. Bull PA (1981) Some fine-grained sedimentation phenomena in caves. *Earth Surf Processes Landforms* 6(1):11–22.
19. An Z, et al. (2000) Asynchronous Holocene optimum of the East Asian monsoon. *Quat Sci Rev* 19(8):743–762.
20. Li X, Hu C, Huang J, Xie S, Baker A (2014) A 9000-year carbon isotopic record of acid-soluble organic matter in a stalagmite from Heshang Cave, central China: Paleoclimate implications. *Chem Geol* 388:71–77.
21. Bar-Matthews M, Ayalon A, Kaufman A, Wasserburg GJ (1999) The eastern Mediterranean paleoclimate as a reflection of regional events: Soreq cave, Israel. *Earth Planet Sci Lett* 166(1–2):85–95.
22. McDermott F (2004) Palaeo-climate reconstruction from stable isotope variations in speleothems: A review. *Quat Sci Rev* 23(7–8):901–918.
23. Zhang YZ, et al. (2013) Holocene paleofloods related to climatic events in the upper reaches of the Hanjiang River valley, middle Yangtze River basin, China. *Geomorphology* 195:1–12.
24. Wang LS, Huang CC, Pang JL, Zha XC, Zhou YL (2014) Paleofloods recorded by slackwater deposits in the upper reaches of the Hanjiang River valley, middle Yangtze River basin, China. *J Hydrol* 519(Part A):1249–1256.
25. Zhou L, et al. (2014) Palaeoflood OSL chronology and its response to climate change in the Yunxi-Yunxian reach in the upper Hangjiang River valley. *Geogr Res* 33(6): 1178–1192.
26. Zha XC, Huang CC, Pang JL, Liu JF, Xue XY (2015) Reconstructing the palaeoflood events from slackwater deposits in the upper reaches of Hanjiang River, China. *Quat Int* 380–381:358–367.
27. Liu T, et al. (2015) Late Pleistocene and Holocene palaeoflood events recorded by slackwater deposits in the upper Hanjiang River valley, China. *J Hydrol* 529(Part 2): 499–510.
28. Guo YQ, et al. (2016) Extraordinary flood events and the response to monsoonal climatic change during the last 3000 years along the middle Yangtze River valley. *Palaeogeogr Palaeoclimatol Palaeoecol* 462:70–84.
29. Zhu C, Yu S, Lu C (1997) The study of Holocene environmental archaeology and extreme flood disaster in the Three Gorges of the Changjiang River and the Jiangnan Plain. *Acta Geogr Sin* 52(3):268–277.
30. Liu Y, et al. (2013) Links between the East Asian Monsoon and North Atlantic climate during the 8,200 year event. *Nat Geosci* 6(2):117–120.
31. Li W, Zhai PM, Cai JH (2011) Research on the Relationship of ENSO and the frequency of extreme precipitation events in China. *Adv Clim Change Res* 2(2):101–107.
32. Jiang T, Zhang Q, Zhu DM, Wu YJ (2006) Yangtze floods and droughts (China) and teleconnections with ENSO activities (1470–2003). *Quat Int* 144(1):29–37.
33. Chen S, et al. (2016) A high-resolution speleothem record of western equatorial Pacific rainfall: Implications for Holocene ENSO evolution. *Earth Planet Sci Lett* 442:61–71.
34. Koutavas A, Joannides S (2012) El Niño-Southern Oscillation extrema in the Holocene and last glacial maximum. *Paleoceanography* 27(4):PA4208.
35. Moy CM, Seltzer GO, Rodbell DT, Anderson DM (2002) Variability of El Niño/Southern Oscillation activity at millennial timescales during the Holocene epoch. *Nature* 420(6912):162–165.
36. Cobb KM, et al. (2013) Highly variable El Niño-Southern Oscillation throughout the Holocene. *Science* 339(6115):67–70.
37. Carré M, et al. (2014) Holocene history of ENSO variance and asymmetry in the eastern tropical Pacific. *Science* 345(6200):1045–1048.
38. Liu ZY, Kutzbach J, Wu LX (2000) Modeling climate shift of El Niño variability in the Holocene. *Geophys Res Lett* 27(15):2265–2268.
39. Liu Z, et al. (2014) Evolution and forcing mechanisms of El Niño over the past 21,000 years. *Nature* 515(7528):550–553.
40. Stuiver M, Braziunas TF (1993) Sun, ocean, climate and atmospheric ^{14}C : An evaluation of causal and spectral relationships. *Holocene* 3(4):289–305.
41. Wang Y, et al. (2005) The Holocene Asian monsoon: Links to solar changes and North Atlantic climate. *Science* 308(5723):854–857.
42. Carslaw KS, Harrison RG, Kirkby J (2002) Cosmic rays, clouds, and climate. *Science* 298(5599):1732–1737.
43. Xu D, et al. (2014) 500-year climate cycles stacking of recent centennial warming documented in an East Asian pollen record. *Sci Rep* 4:3611.
44. Cheng H, et al. (2015) The climate variability in northern Levant over the past 20,000 years. *Geophys Res Lett* 42(20):8641–8650.
45. Chapman MR, Shackleton NJ (2000) Evidence of 550-year and 1000-year cyclicity in North Atlantic circulation patterns during the Holocene. *Holocene* 10(3):287–291.
46. Stuiver M, et al. (1998) INTCAL98 radiocarbon age calibration, 24000–0 cal BP. *Radiocarbon* 40(3):1041–1083.
47. Jiang DB, et al. (2015) Paleoclimate modeling in China: A review. *Adv Atmos Sci* 32(2): 250–275.
48. Kirov B, Georgieva K (2002) Long-term variations and interrelations of ENSO, NAO and solar activity. *Phys Chem Earth* 27(6–8):441–448.
49. Strehlau JH, et al. (2014) Simple and efficient separation of magnetic minerals from speleothems and other carbonates. *J Sediment Res* 84(11):1096–1106.
50. Kruijer PP, Dekkers MJ, Heslop D (2001) Quantification of magnetic coercivity components by the analysis of acquisition curves of isothermal remanent magnetisation. *Earth Planet Sci Lett* 189(3–4):269–276.
51. Guyodo Y, et al. (2006) Rock magnetic, chemical and bacterial community analysis of a modern soil from Nebraska. *Earth Planet Sci Lett* 251(1–2):168–178.

Supporting Information

Zhu et al. 10.1073/pnas.1610930114

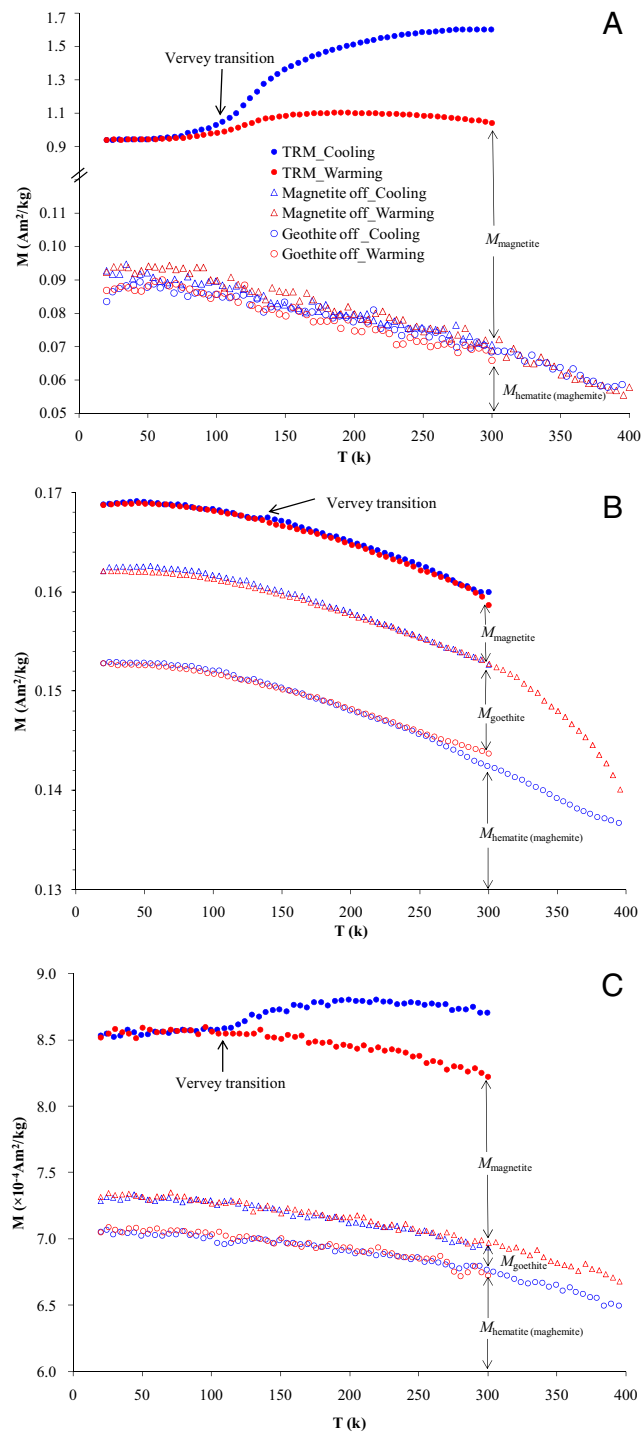


Fig. S1. Low-temperature behavior of magnetic extracts from stalagmite HS4 specimens. We used a four-stage protocol that allows distinguishing of remanence held by goethite and hematite from that held by magnetite (51). In the first stage, a TRM was imparted to each specimen at a 2.5-T dc field during a circle warming from 300 K to 400 K and then cooling from 400 K to 300 K. Then the remanence of each specimen was measured during thermal cycling in a zero field environment from 300 K to 10 K and back to 300 K (“TRM_Cooling” and “TRM_Warming”). This remanence represents the combined contributions from goethite, hematite, and magnetite. In the second stage, the sample was removed from the MPMS and demagnetized using an AF with a peak intensity of at 200 mT to remove nearly all of the remanence carried by magnetite. In the third stage, the specimen was inserted into the MPMS again, and its remanent magnetization was measured during thermal cycling in a zero-field environment from 300 K to 10 K, and then warmed to 400 K (“Magnetite off_Cooling” and “Magnetite off_Warming”). This stage measures the remanence of goethite and hematite, and then ultimately demagnetizes any goethite in the sample by warming from 300 K to 400 K. In the fourth stage, the specimens were measured at zero field during cooling from 400 K to 10 K and then warming to 300 K (“Goethite off_Cooling” and “Goethite off_Warming”). $M_{\text{magnetite}}$, M_{goethite} , and $M_{\text{hematite (maghemite)}}$ indicate the magnetic remanence carried by magnetite, goethite, and hematite (probably company with maghemite), respectively. Strong particles extracted from the sample with (A) high, (B) low, and (C) medium $\text{IRM}_{\text{soft-flux}}$ values.

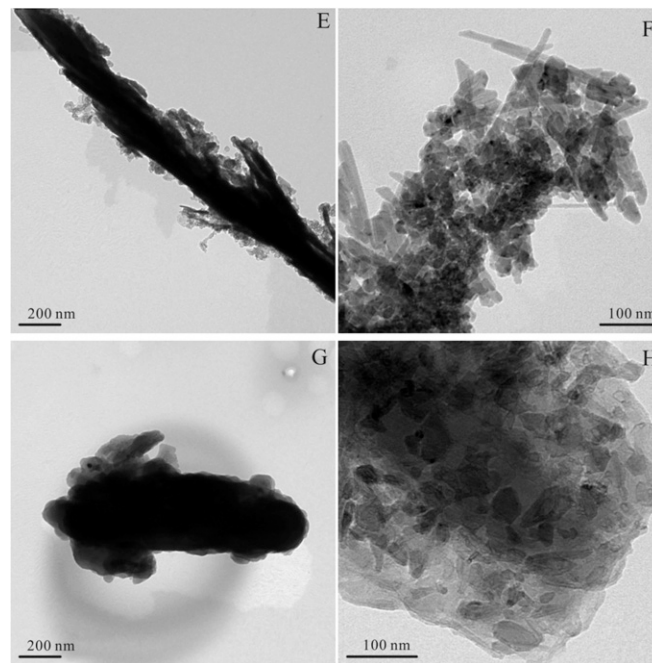


Fig. S2. SEM and TEM micrograph of magnetic minerals extracted from stalagmite HS4. (A–D) SEM micrographs and EDS spectrums of extracted magnetite particles with etch pits and plumose textures. No evidence of shrinkage cracks associated with maghemitization are present. (E–H) TEM micrographs. (E) Needle-like particles with adsorbed, nanometer-scale, Fe-oxide minerals. (F) Needle-shaped goethite and irregularly shaped nanometer particles. (G) An $\sim 1\text{-}\mu\text{m}$, rounded magnetite with $\sim 200\text{-nm}$ minerals adhering to its surface. (H) Irregularly shaped, $<100\text{-nm}$ particles in a clay-rich matrix.

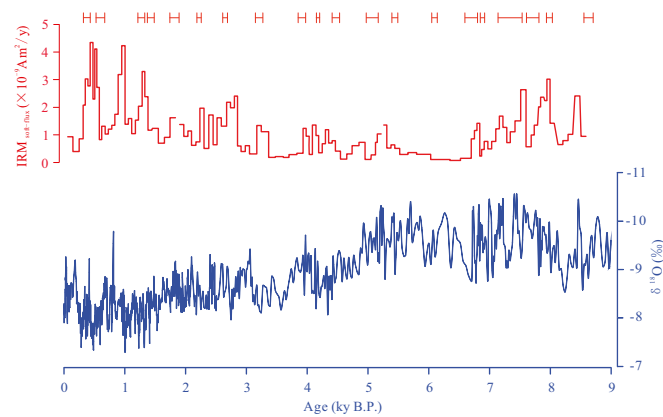


Fig. S3. Comparison of $IRM_{\text{soft-flux}}$ (red curve) and oxygen isotope sequences (blue curve, from ref. 12), both from stalagmite HS4. Error (2σ) of U–Th dating is shown as separate red segments at the top of the figure.

Table S1. IRM_{soft_flux} of 115 stalagmite specimens

| Specimen ID | Age (years before 1950) | IRM _{soft_flux} (Am ² /yr) | Specimen ID | Age (years before 1950) | IRM _{soft_flux} (Am ² /yr) |
|-------------|-------------------------|--|-------------|-------------------------|--|
| 1 | 100-176 | 9.34E-10 | 59 | 4041-4086 | 3.01E-10 |
| 2 | 180-249 | 4.11E-10 | 60 | 4089-4145 | 1.36E-09 |
| 3 | 249-318 | 8.79E-10 | 61 | 4147-4193 | 9.85E-10 |
| 4 | 322-358 | 2.08E-09 | 62 | 4193-4249 | 3.65E-10 |
| 5 | 358-392 | 3.03E-09 | 63 | 4249-4302 | 7.01E-10 |
| 6 | 398-434 | 2.76E-09 | 64 | 4302-4348 | 1.19E-09 |
| 7 | 441-475 | 4.34E-09 | 65 | 4356-4409 | 7.13E-10 |
| 8 | 475-511 | 2.29E-09 | 66 | 4409-4462 | 8.01E-10 |
| 9 | 509-545 | 4.13E-09 | 67 | 4462-4550 | 4.18E-10 |
| 10 | 547-582 | 2.72E-09 | 68 | 4550-4649 | 1.33E-10 |
| 11 | 581-621 | 8.33E-10 | 69 | 4654-4739 | 3.28E-10 |
| 12 | 621-676 | 1.33E-09 | 70 | 4749-4848 | 6.24E-10 |
| 13 | 679-731 | 1.04E-09 | 71 | 4853-4948 | 7.35E-10 |
| 14 | 734-789 | 1.23E-09 | 72 | 4950-5047 | 1.11E-10 |
| 15 | 789-841 | 1.36E-09 | 73 | 5064-5124 | 2.91E-10 |
| 16 | 844-898 | 1.76E-09 | 74 | 5124-5149 | 7.40E-10 |
| 17 | 898-956 | 3.20E-09 | 75 | 5156-5219 | 1.04E-09 |
| 18 | 956-1005 | 4.25E-09 | 76 | 5256-5307 | 1.36E-09 |
| 19 | 1014-1065 | 1.40E-09 | 77 | 5313-5376 | 5.23E-10 |
| 20 | 1069-1121 | 1.61E-09 | 78 | 5376-5439 | 6.44E-10 |
| 21 | 1121-1173 | 1.06E-09 | 79 | 5439-5523 | 5.15E-10 |
| 22 | 1173-1225 | 1.55E-09 | 80 | 5505-5651 | 2.94E-10 |
| 23 | 1226-1284 | 2.06E-09 | 81 | 5663-5798 | 3.72E-10 |
| 24 | 1284-1333 | 3.30E-09 | 82 | 5798-5915 | 3.15E-10 |
| 25 | 1336-1384 | 2.39E-09 | 83 | 5915-6031 | 3.15E-10 |
| 26 | 1387-1454 | 1.17E-09 | 84 | 6031-6167 | 1.24E-10 |
| 27 | 1454-1552 | 1.26E-09 | 85 | 6167-6349 | 1.16E-10 |
| 28 | 1556-1654 | 7.08E-10 | 86 | 6349-6513 | 8.48E-11 |
| 29 | 1654-1752 | 9.25E-10 | 87 | 6513-6695 | 1.70E-10 |
| 30 | 1752-1834 | 1.64E-09 | 88 | 6695-6751 | 8.70E-10 |
| 31 | 1902-1973 | 1.38E-09 | 89 | 6751-6791 | 1.17E-09 |
| 32 | 1976-2041 | 9.62E-10 | 90 | 6793-6830 | 1.43E-09 |
| 33 | 2041-2105 | 1.15E-09 | 91 | 6830-6870 | 2.34E-10 |
| 34 | 2105-2171 | 6.36E-10 | 92 | 6870-6913 | 4.84E-10 |
| 35 | 2176-2239 | 7.52E-10 | 93 | 6913-6974 | 7.72E-10 |
| 36 | 2239-2310 | 1.98E-09 | 94 | 6974-7034 | 4.95E-10 |
| 37 | 2310-2381 | 5.08E-10 | 95 | 7034-7095 | 7.73E-10 |
| 38 | 2388-2452 | 1.73E-09 | 96 | 7095-7156 | 1.23E-09 |
| 39 | 2452-2523 | 6.56E-10 | 97 | 7156-7216 | 1.69E-09 |
| 40 | 2523-2591 | 1.62E-09 | 98 | 7216-7277 | 1.28E-09 |
| 41 | 2591-2672 | 1.32E-09 | 99 | 7277-7338 | 7.30E-10 |
| 42 | 2678-2737 | 2.18E-09 | 100 | 7338-7419 | 1.12E-09 |
| 43 | 2740-2799 | 1.99E-09 | 101 | 7419-7514 | 1.51E-09 |
| 44 | 2799-2855 | 2.41E-09 | 102 | 7518-7596 | 2.64E-09 |
| 45 | 2855-2914 | 5.99E-10 | 103 | 7596-7683 | 5.68E-10 |
| 46 | 2918-2986 | 4.13E-10 | 104 | 7683-7736 | 9.96E-10 |
| 47 | 2989-3048 | 6.28E-10 | 105 | 7736-7785 | 1.36E-09 |
| 48 | 3051-3110 | 3.11E-10 | 106 | 7798-7835 | 2.03E-09 |
| 49 | 3110-3170 | 3.21E-10 | 107 | 7847-7884 | 2.37E-09 |
| 50 | 3170-3242 | 1.35E-09 | 108 | 7899-7937 | 2.25E-09 |
| 51 | 3247-3365 | 1.13E-09 | 109 | 7942-7976 | 3.02E-09 |
| 52 | 3365-3476 | 1.98E-10 | 110 | 7995-8059 | 1.43E-09 |
| 53 | 3488-3611 | 2.31E-10 | 111 | 8118-8199 | 6.70E-10 |
| 54 | 3611-3705 | 1.94E-10 | 112 | 8204-8285 | 8.02E-10 |
| 55 | 3711-3828 | 2.95E-10 | 113 | 8290-8365 | 1.03E-09 |
| 56 | 3834-3935 | 3.40E-10 | 114 | 8397-8472 | 2.41E-09 |
| 57 | 3935-3988 | 1.24E-09 | 115 | 8499-8580 | 9.62E-10 |
| 58 | 3988-4038 | 9.62E-10 | | | |